Two-Step Optimum Design Process of PMSM to Improve Driving Efficiency and Harmonics of Lightweight Electric Vehicle

So-Yeon Im, Kyoung-Soo Cha, Yun-Jae Won, *Graduate Student Member, IEEE*, Yun-Yong Choi, and Myung-Seop Lim, *Member, IEEE*

***Abstract*—Urban lightweight electric vehicles (EVs) for personal mobility have the advantage of being convenient and economical. Vehicles with low vibrations and high energy efficiency are suitable for use as urban electric vehicles. The torque ripple of the motor that induces the vibration of the EV can be improved by reducing the harmonics of the magnetic flux density. The energy efficiency of an EV can be improved by increasing the efficiency at the main operating points (MOPs) by considering the driving cycle. Through the proposed design process, optimization was performed to improve the harmonic characteristics of a high-efficiency lightweight EV with a stator chamfer and rotor notch structure. The harmonics of the magnetic flux density due to the teeth and slots are improved through the stator chamfer, and the fundamental component of the magnetic flux density is increased through the rotor notch structure. The optimum model designed through the proposed design method has improved the efficiency at the MOPs and harmonic characteristics.**

***Index Terms*—Electric vehicle, motor, optimum design, rotor notch, stator chamfer.**

I. Introduction

With the fuel crisis and increasing importance of environmental protection, the development of electric vehicles (EVs) is accelerating [1], [2], [3], [4]. EVs with high efficiency and torque density have the potential to provide solutions for sustainable personal mobility in the future [5]. To achieve high performance, interior permanent magnet synchronous motors (IPMSMs) have been studied as electric propulsion systems for lightweight EVs [6], [7]. Lightweight EVs for personal mobility are city cars with short driving ranges. Therefore, economy and comfort are considered when designing lightweight EVs. In addition, lightweight EVs with high energy efficiency are economical. As a vehicle with low vibration provides convenience to vehicle occupants, a traction motor should be designed such that the torque ripple that causes vibration is small. An IPMSM has a high torque density because magnetic torque and reluctance torque are generated, but the torque ripple is significant owing to the difference in impedance between the d-axis and q-axis that creates the reluctance torque [8]. The cogging torque and torque ripple of the traction motor that causes vibration in the EV system can be reduced by improving the harmonics of the magnetic flux density. Applying a stator chamfer and rotor notch structures to a traction motor can reduce harmonics while maintaining its performance [1]. For a lightweight EV with a specific driving cycle, the main operating points (MOPs) with high energy consumption are identified through a vehicle driving simulation, and the economic efficiency can be secured by improving the efficiency at the MOPs of the traction motor. As motor efficiency depends on parameters such as bridge and rib thickness and permanent magnet (PM) position, the optimum design for the motor shape is determined.

In previous studies, a rotor notch and skew structure were applied to reduce the cogging torque and torque ripple of an electric motor [9], [10], [11], [12]. However, the skewed rotor increases the manufacturing cost due to the segmented magnets and has a large effect on axial leakage. The rotor core notch structure can reduce the harmonics by improving the trapezoidal waveform of the air-gap magnetic flux density. In addition, studies on the design of high-performance EV traction motors and characteristics of vehicle systems are being actively conducted [13], [14], [15], [16]. A traction motor for battery EVs with a reduced radial force by applying a rotor with asymmetric PM positions was designed in [17]. The flux-concentrated PM rotor, which combines the spoke type and Halbach PM arrangement proposed in [18], increases the magnitude of the air gap flux density, thereby improving the power and torque density of the traction motor for EV applications. The dual-rotor motor with

Manuscript received 24 October 2022; revised 28 February 2023 and 1 May 2023; accepted 5 August 2023. Date of publication 10 August 2023; date of current version 22 November 2023. Paper 2022-EMC-0981.R2, presented at the 2022 IEEE Transportation Electrification Conference & Expo, Anaheim, CA, USA, Jun. 15–17, and approved for publication in the IEEE TRANSACTIONS ON INDUSTRY APPLICATIONS by the Electric Machines Committee of the IEEE Industry Applications Society [DOI: 10.1109/ITEC53557.2022.9813766]. *(Corresponding author: Myung-Seop Lim.)*

So-Yeon Im is with the Department of Automotive Engineering (Automotive-Computer Convergence), Hanyang University, Seoul 04763, South Korea (e-mail: soyeon96@hanyang.ac.kr).

Kyoung-Soo Cha is with the Korea Institute of Industrial Technology, Deagu 42994, South Korea (e-mail: kscha@kitech.re.kr).

Yun-Jae Won and Myung-Seop Lim are with the Department of Automotive Engineering, Hanyang University, Seoul 04763, South Korea (e-mail: w961227@hanyang.ac.kr; myungseop@hanyang.ac.kr).

Yun-Yong Choi is with the Department of Automotive Engineering, Hanyang University, Seoul 04763, South Korea, and also with the DRIVETECH Co., LTD, Bucheon 14558, South Korea (e-mail: gipson12@drivetech.kr).

Color versions of one or more figures in this article are available at https://doi.org/10.1109/TIA.2023.3303860.

Digital Object Identifier 10.1109/TIA.2023.3303860

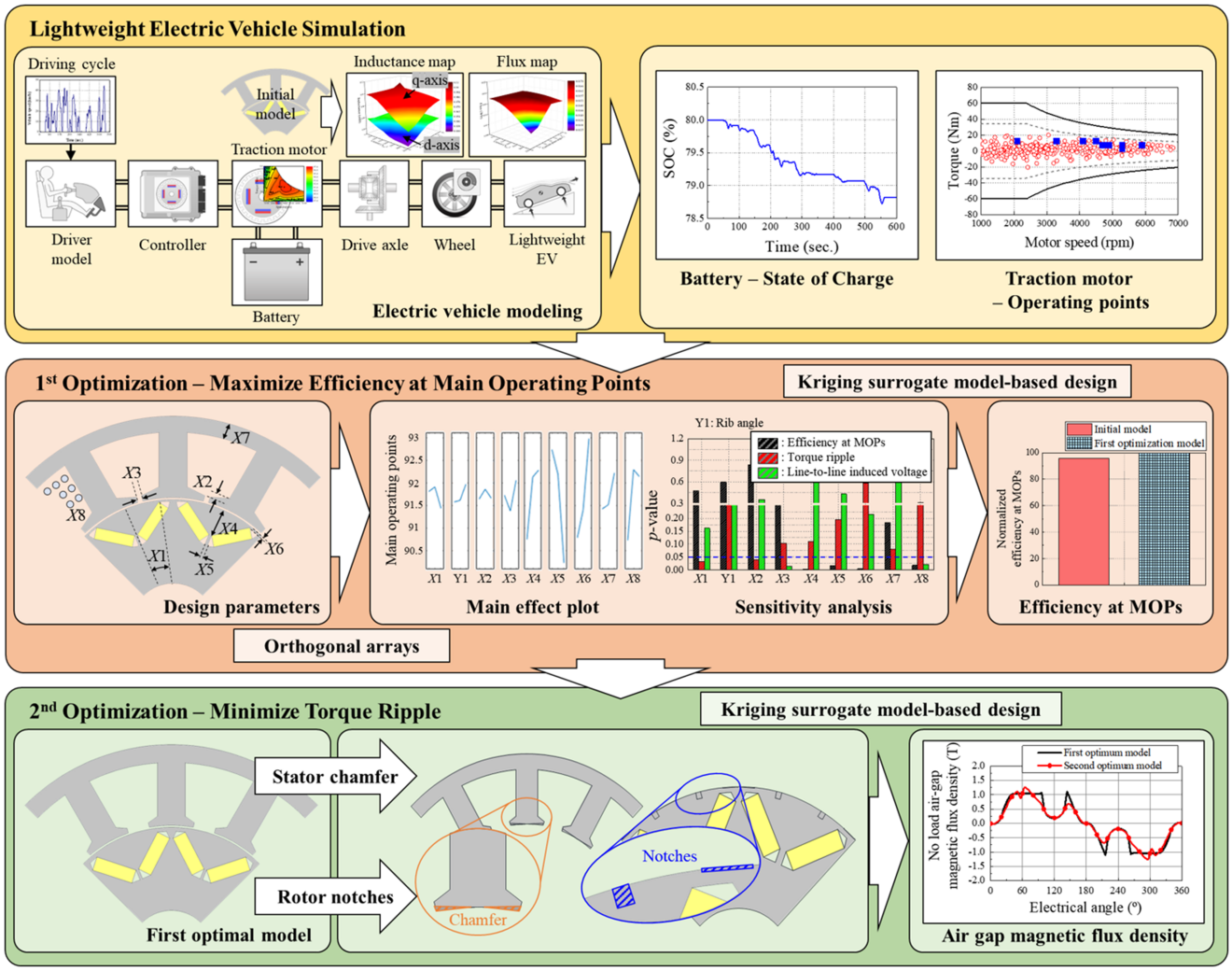

Fig. 1. Proposed design process.

synchronous and asynchronous rotors in [19] can be utilized to satisfy the various driving requirements of EVs. In another study [20], an electric propulsion system combining an IPMSM and a PM-assisted synchronous reluctance motor was proposed to increase traction performance and energy efficiency, and the characteristics of the vehicle system for the urban driving cycle were compared. Sun et.al [21] optimized the PM hub motor geometry for an EV used for campus patrols with a specific driving cycle. A traction motor design that satisfies the maximum torque at the rated speed determined through a specific driving cycle was derived. However, studies determining MOPs and performing stepwise optimization to achieve high energy efficiency and reduced harmonics of a traction motor for lightweight EVs can reduce computation time and provide a useful solution for studying traction motors for EV applications. Determining the MOPs of a motor through EV simulation with high accuracy in predicting motor characteristics according to the driving cycle is closely related to designing an optimum motor model.

In this study, a two-step optimization of the motor shape was performed to improve the efficiency of the MOPs and harmonic characteristics of the lightweight EV traction motor. The MOPs were determined as operating points with a high energy consumption ratio through an EV driving simulation for the driving cycle. In the first step, the motor shape parameters that affect motor performance, including the efficiency at the MOPs determined through sensitivity analysis, are optimized. In the second step, the harmonics of the first optimum model are analyzed, and the design parameters for the stator chamfer and rotor notch structure are optimized to improve the harmonics. Kriging surrogate model-based optimization was performed to determine the optimum model. The optimum model designed using the proposed method in Fig. 1 has improved efficiency at MOPs and harmonic characteristics compared with the initial model.

The organization of this article is as follows. Section II, the MOPs of the traction motor are estimated by considering the driving cycle through an EV simulation. Next, a two-step optimum design process for maximizing the efficiency at the MOPs of the traction motor and improving the harmonics is proposed, and optimizations are performed in Section III. In Section IV, a load test was conducted for experimental verification of the

TABLE I
SPECIFICATIONS OF THE TARGET TRACTION MOTOR

Parameter	*Value*	*Unit*
DC link voltage	66	V_{DC}
Current limit	400	A_{rms}
Switching frequency	8	kHz
Maximum power	15	kW
Maximum torque	60	Nm
Maximum rotational speed	7000	rpm
Stator / rotor outer diameter	150 / 90	mm
Stack length	110	mm
PM thickness / width	5 / 15	mm

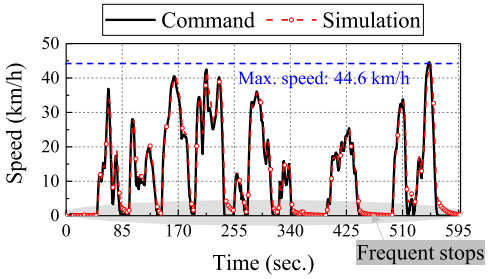

Fig. 2. Target driving cycle and vehicle speed according to time.

TABLE II
SPECIFICATIONS OF THE TARGET VEHICLE

Parameter	*Value*	*Unit*
Vehicle mass (Gross train)	690	kg
Wheel radius (Front / rear)	125 / 145	mm
Wheelbase	1686	mm
Vehicle length / width	2338 / 1094	mm
Vehicle drag coefficient	0.64	-
Gear ratio	9.23	-
Gear efficiency	95	%
Air density	1.28	kg/m^3
Gravitational accleration	9.81	m/s^2
Rolling resistance coefficient	0.01	-
Maximum DC link voltage	72	V_{DC}

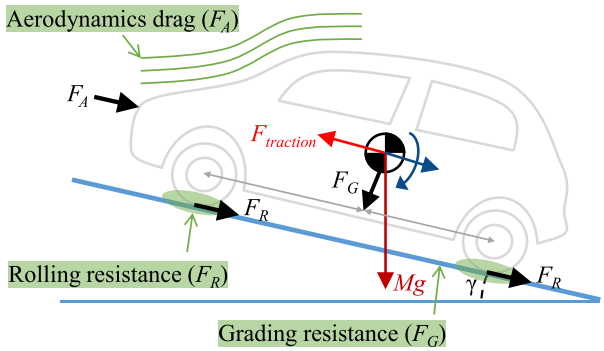

Fig. 3. Dynamic loads diagram of the vehicle.

prototypes. Finally, the conclusions of the study are presented in Section V.

II. LIGHTWEIGHT ELECTRIC VEHICLE SIMULATION

The target vehicle was a lightweight EV for personal mobility, and the specifications of the traction motor are listed in Table I. Considering the switching frequency and maximum speed of the traction motor, the number of poles was determined as eight. To minimize the end-coil height, the number of slots was determined to be 12 with concentrated windings. An initial model was developed for the IPMSM with V-shaped magnets to satisfy the maximum torque. The initial model was used in an EV simulation to estimate the operating points of the traction motor for the driving cycle as shown in Fig. 1. The target driving cycle in Fig. 2 is the New York City Cycle (NYCC)—a low-speed urban driving cycle with frequent stops.

A. Vehicle Modeling and Driving Condition

In vehicle modeling, the driver model compares the commanded driving cycle with the vehicle speed and transmits a deceleration or acceleration command to the controller. The controller delivers the required torque to the traction motor for deceleration or acceleration. The controller calculates the torque command based on the traction motor's torque versus speed characteristics and limits the maximum torque, preventing overload during simulation. The lithium-ion battery model supplies energy to the traction motor, and power is transmitted to the drive axle through the reduction gear [1]. The battery model utilizes data on resistors and capacitors corresponding to one cell, and the number of cells in series is adjusted to supply the voltage required to drive the traction motor. The resistors and capacitors of the battery change with the state of charge [22]. To reflect the characteristics of the traction motor, the d-and q-axis inductance and flux maps for the current and current phase angle are derived through finite element analysis. The motor parameter maps analyzed in detail constitute a d-and q-axis equivalent circuit considering iron loss. The characteristics of the traction motor are calculated through the voltage, current, and torque equations based on the d-and q-axis equivalent circuits [3]. Applying maximum torque per ampere (MTPA) control, the current phase angle is calculated so that the torque generated per current is maximized [23]. The torque versus speed characteristics and efficiency of the traction motor calculated through the equations are reflected in the lightweight EV simulation. Within the limiting condition of the input power, the peak performance curve is derived, and the rated current density is limited to 5 A_{rms}/mm^2 considering the natural air-cooled motor to prevent damage due to overload. The specifications of the target EV are listed in Table II. Since the EV simulation was based on a mathematical model, the dynamic axle loads in Fig. 3 were calculated and reflected [24]. Dynamic loads consist of

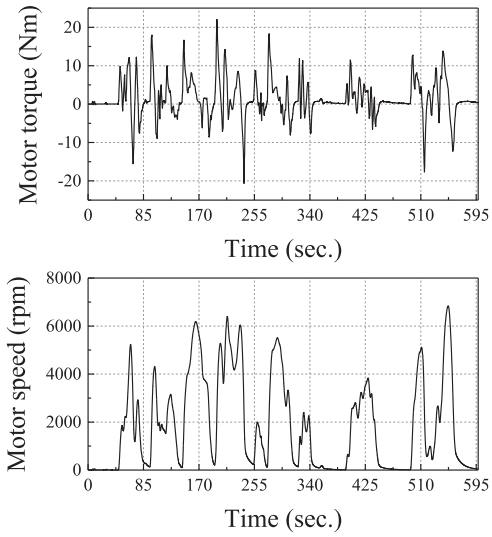

Fig. 4. Motor torque and speed according to target driving cycle.

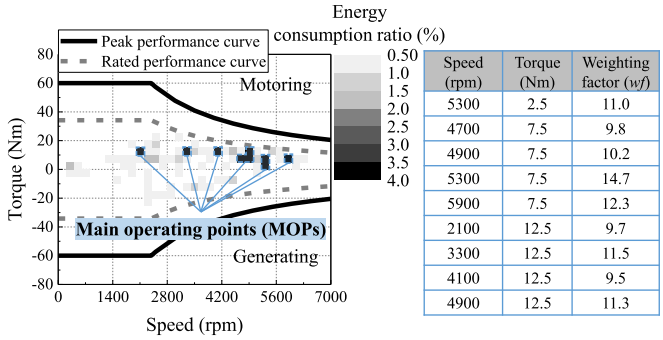

Speed (rpm)	Torque (Nm)	Weighting factor (*wf*)
5300	2.5	11.0
4700	7.5	9.8
4900	7.5	10.2
5300	7.5	14.7
5900	7.5	12.3
2100	12.5	9.7
3300	12.5	11.5
4100	12.5	9.5
4900	12.5	11.3

Fig. 5. Main operating points and weighting factors [1].

aerodynamic drag owing to friction, rolling resistance owing to hysteresis of the tire material, and grading resistance acting on the vehicle going up the slope. Based on the longitudinal dynamic equation of the lightweight EV, the torque required for the traction motor can be calculated as:

$$T = \frac{r}{\eta_g G}\left(Ma + \frac{1}{2}\rho C_d A_f V^2 + f_r Mg\cos\gamma + Mg\sin\gamma\right) \tag{1}$$

where r is the wheel radius, η_g is the gear efficiency, G is the gear ratio, M is the vehicle mass, a is the longitudinal vehicle acceleration, ρ is the air density, C_d is the drag coefficient of the vehicle, A_f is the frontal area of the vehicle, V is the vehicle speed, f_r is the rolling resistance coefficient, g is gravitational acceleration, and γ is the slope angle. Fig. 4 shows the motor torque and speed according to the driving cycle. The MOPs were determined using the motor torque and speed profiles estimated through the EV simulation.

B. Determination of Main Operating Points

A design that increases motor efficiency at all operating points during the target driving cycle is effective in increasing the energy efficiency of the target vehicle. In addition, a design that repeatedly performs electromagnetic finite element analysis (FEA) and EV simulation according to a change in the motor shape to improve the economics of the target vehicle is also useful. However, in the optimum design process, energy efficiency analysis reflecting all operating points and coupling analysis of electromagnetic FEA and EV simulations take a long time to calculate. Accordingly, the MOPs of the traction motor were determined to shorten the computation time and achieve a cost-effective optimum design. Among the methods for determining the MOPs of the traction motor, selecting operating points with a high-energy consumption ratio and increasing the efficiency of those points is effective in improving the mileage of the target vehicle. Therefore, the MOPs of the traction motor considering NYCC are determined as operating points with a high energy-consumption ratio, and the energy consumption ratio is calculated as follows:

$$\text{Energy consumptionratio}\,(\varepsilon) = \frac{(T_i\omega_i)\,n_i}{\sum_{i=1}^{k}(T_i\omega_i)\,n_i} \tag{2}$$

where k is the total number of operating regions, T_i is the torque of the traction motor in the ith operating region, ω_i is the speed of the traction motor in the ith operating region, and n_i is the number of operating points in the ith operating region. Fig. 5 shows all operating points of the traction motor through the EV simulation, and the MOPs are the operating points of the traction motor, where the energy consumption ratio is 3.5% or higher [1]. The weighting factors in Fig. 5 are determined according to the ratio of each MOP to the sum of the energy consumption ratios of the MOPs and are expressed as

$$\text{Weighting factor}\,(wf) = \frac{\varepsilon_j}{\sum_{j=1}^{9}\varepsilon_j} \tag{3}$$

where ε_j is the energy-consumption ratio at the jth MOP. As a result, the main operational efficiency of the traction motor calculated by multiplying the efficiency of the corresponding MOP by the weighting factor is as follows:

$$\eta_{MOP} = \sum_{j=1}^{9}\frac{\eta_{mj} wf_j}{100} \tag{4}$$

where η_{mj} is the motor efficiency, and wf_j is the weighting factor at the jth MOP. The motor efficiency is calculated by reflecting the iron loss and armature copper loss. The traction motor is controlled to achieve the maximum torque per ampere operation [3], [23].

III. Two-Step Optimum Design Process

The kriging surrogate model-based optimization was performed in stages to improve the main operating efficiency and harmonic characteristics of the traction motor. As the kriging surrogate model has a high prediction accuracy for nonlinearity, it is applied to the optimum design of motors with magnetic and mutual saturation characteristics [25], [26], [27]. In the first optimization, a sensitivity analysis is performed to determine design parameters sensitive to motor performance, such as the main operating efficiency, maximum torque, and maximum

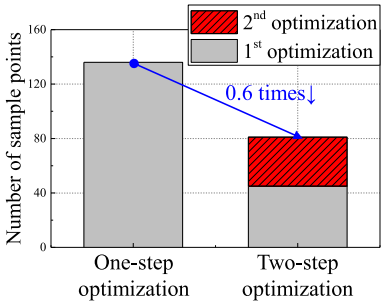

Fig. 6. Number of sample points.

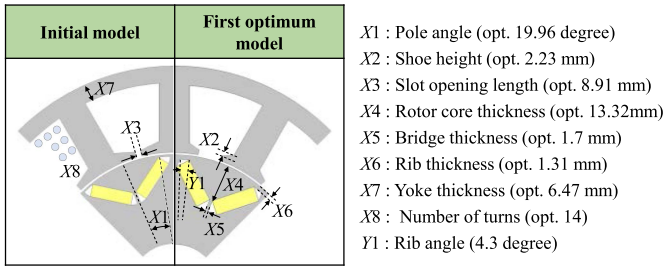

Fig. 7. Design parameters in the first optimization and structure of the initial model and first optimum model [1].

power. Then, the design variables determined through sensitivity analysis are optimized to maximize the efficiency of the MOPs. In the second optimization, the design parameters for the stator chamfer and rotor notches were optimized to improve the harmonics of the first optimum model. Stepwise optimization can shorten the computation time required for design. This is because many sample points are required to secure the reliability of the optimization performed only once for many design variables. The electromagnetic FEA conducted at each sample point requires a lot of computation time. Since stepwise optimization is performed for independent objective functions by classifying design variables, sample points of the design of experiments (DOE) can be reduced. The number of initial sample points is calculated as follows [28]

$$N_s = \frac{(N_d + 1)(N_d + 2)}{2} \tag{5}$$

where N_d is the number of design variables. The increased number of sample points can improve the accuracy of the kriging surrogate model. As shown in Fig. 6, the two-step optimization can reduce the number of sample points by 0.6 times.

A. *First Optimization: Maximization of Efficiency at Main Operating Points*

The objective function of the first optimization is to maximize the motor efficiency at the MOPs. The constraint is to satisfy the electrical specifications, maximum torque, and maximum power. In addition, the torque ripple at the point of maximum torque is limited. The first optimization problem is expressed as follows:

$$\begin{aligned} &\text{maximize } \eta_{MOP} \\ &\text{subject to } V_{\text{line-to-line}} \le V_{\text{line-to-linemax}} \& J \le J_{\max} \\ &\qquad T \ge T_{\text{target}} \& P \ge P_{\text{target}} \\ &\qquad T_{\text{ripple}} \le T_{\text{ripplelimit}} \end{aligned} \tag{6}$$

where $V_{\text{line-to-line}}$ is the line-to-line induced voltage, $V_{\text{line-to-line max}}$ is the maximum line-to-line induced voltage, J is the current density, $J_{\max}$ is the maximum current density, T is the torque, T_{target} is the target maximum torque at the base speed, P is the power, P_{target} is the target maximum power at the maximum speed, T_{ripple} is the torque ripple at the base speed, and $T_{\text{ripple limit}}$ is the limit value of torque ripple. Sensitivity analysis was performed to determine the performance-sensitive design variables among the shape parameters of the traction motor. In the sensitivity analysis using the orthogonal array, the motor shape parameters are shown in Fig. 7, and the performances are the efficiency at the MOPs, maximum torque, maximum power, line-to-line inducted voltage, and torque ripple at the base speed. The main effect plot of Fig. 8(a) shows the change in the efficiency at the MOPs according to the level of the motor shape parameters. The efficiency at the MOPs with respect to the change in the motor shape parameters has non-linearity. Therefore, a sensitivity analysis should be performed at a 3-level or higher. Through main effect plots, $X4$, $X5$, $X6$, and $X8$, which are sensitive to the efficiency at the MOPs, are determined as design variables. An analysis of variance (ANOVA) is performed to determine which design variables are sensitive to maximum torque, torque ripple at base speed, and maximum line-to-line induced voltage. An ANOVA is a method of quantitatively analyzing the sensitivity of design variables to performance using the F-distribution considered through the comparison of variance between groups and within groups. The F-distribution is a probability distribution with a variance ratio as a variable. The p-value is calculated from the F-distribution. The p-value in Fig. 8(b) indicates the probability that a specific parameter does not affect performance. In the first optimization, the motor shape parameters with a p-value less than 0.05 are determined as design variables. The p-value is an index indicating the degree to which errors are tolerated, and it means that the sensitivity to the performance of design variables is high with a reliability of 95% or more. Therefore, the lower the p-value of the motor shape parameter for performance, the higher the sensitivity it is. Through p-value, $X1$, $X2$, and $X3$ are additionally determined as design variables. The contribution ratio expresses the degree to which a specific shape parameter affects performance and can identify the relative sensitivity of the design variables to performance. Among the shape parameters excluding the design variables determined through main effect plots and p-value, $X7$ is a key design variable related to reluctance and saturation in motor design. The saturation of the stator affects maximum torque. Therefore, $X7$ is determined as a design variable by considering the contribution ratio to maximum torque in Fig. 8(c). As a result of the sensitivity analysis, a total of eight design variables from $X1$ to $X8$ were determined for the first optimization, considering the main effect plot, p-value, and contribution ratio. The DOE

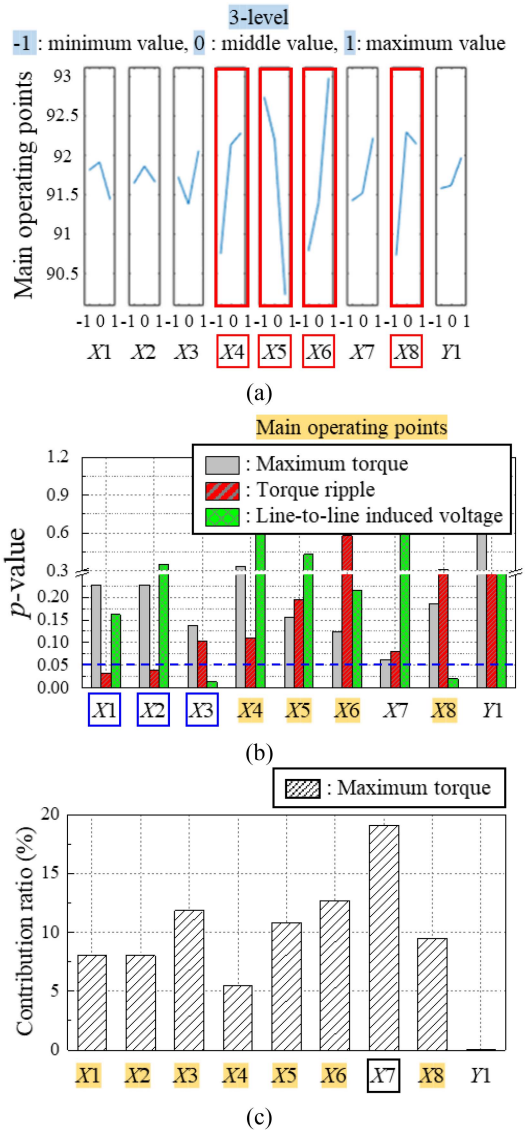

Fig. 8. Results of sensitivity analysis: (a) main effect plot, (b) p-value, and (c) contribution ratio.

using optimal Latin hypercube sampling was performed on the determined design variables. In the first kriging surrogate model-based optimization, the number of sample points was determined to be 180, considering the number and range of the design variables. Sequential quadratic programming (SQP) was applied to derive the optimum design results. As shown in Fig. 9, the SQP method iteratively evaluates the gradient of the objective function with respect to parameters to solve a nonlinear problem [29]. The performance according to the design variables was analyzed through electromagnetic FEA to reflect the nonlinear magnetic saturation of the motor core. To estimate the iron loss, the harmonics are analyzed for the magnetic flux density of one electrical period, calculated with the FEA performed on one element. Based on the measured iron loss data, the iron loss of one element is found considering the operating frequency and harmonic order. This process is repeated for all elements, and the sum of the iron losses for each

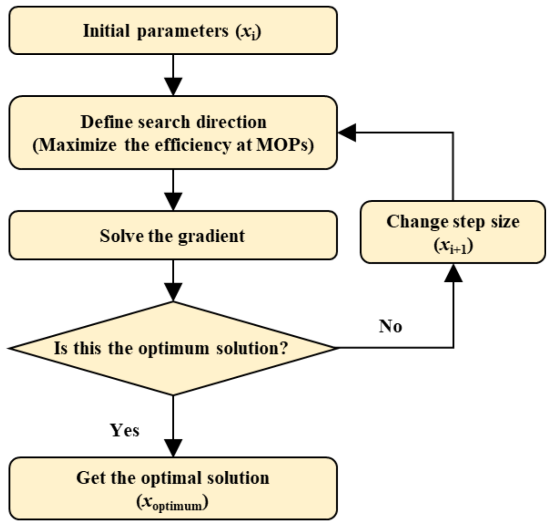

Fig. 9. Sequential quadratic programming.

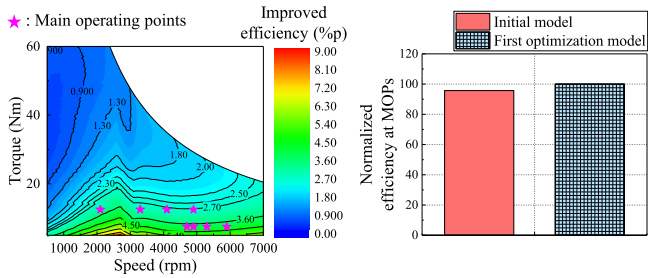

Fig. 10. Efficiency (a) improved efficiency map and (b) normalized efficiency at MOPs.

element is calculated as the total iron loss of the motor. Fig. 7 shows the first optimum model for the geometry, excluding the stator chamfer and rotor notch structures. The first optimization model improved the motor efficiency including the efficiency at MOPs. Fig. 10 shows the improved efficiency of the first optimization model compared to the initial model. In addition, the first optimum model designed through the proposed design process increases the efficiency at MOPs by 4.3%p more than the initial model.

B. Second Optimization: Improved Design With Stator Chamfer and Rotor Notches Structures

A second optimization was performed to improve the harmonic characteristics. Various structures can be applied to reduce the harmonics of the air-gap magnetic flux density owing to the stator tooth and slot structures and field source [30], [31], [32], [33]. Although a skewed rotor can be effective in improving harmonic characteristics, axial forces can be generated that cause vibration in the motor system [10]. In addition, the skew structure reduces electromagnetic excitation forces and is effective in offsetting cogging torque and torque ripple [11], [34]. However, 3-dimensional (3D) FEA is required to predict axial leakage due to a skewed rotor and to optimize the optimal skew angle for harmonic reduction. Since 3D FEA increases the

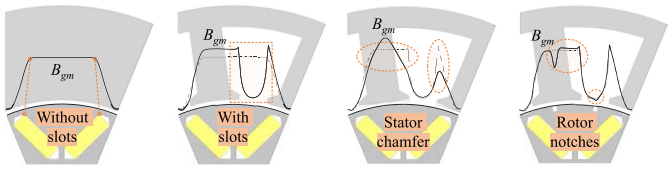

Fig. 11. Waveform of air-gap magnetic flux density according to application of stator chamfer and rotor notches structures.

computation time, the harmonics of the traction motor were improved by applying the 2-dimensional stator chamfer and rotor notch structures in the second optimization. The stator chamfer in Fig. 11 reduces the spatial change rate of the air gap reluctance, thereby reducing the harmonics of the air-gap magnetic flux density. The rotor notch structures shown in Fig. 11 reduce the distribution of the magnetic flux density along the q-axis, thereby reducing the harmonics of the air-gap magnetic flux density. As the harmonics of air-gap flux density are reduced, the cogging torque and torque ripple are reduced. However, the effective air-gap length is increased owing to the stator chamfer and rotor core notched structure. Therefore, the fundamental component of the back EMF was also reduced. For this reason, a rotor rib notch structure is applied to increase the reduced fundamental component of the back EMF.

Under load conditions, the harmonic characteristics of the air-gap magnetic flux density differ depending on the armature current and current phase angle. In addition, the rotor rib notch structure reduces the leakage flux but increases the mechanical stress as the rib thickness decreases. The minimum rib thickness should be limited to ensure rotational stiffness. As the harmonics of the air-gap magnetic flux density affect the torque ripple, the second optimization problem for the stator chamfer and rotor notch structures is as follows:

$$\begin{aligned} &\text{minimize } T_{\text{ripple}} \\ &\text{subject to } T \geq T_{\text{target}} \\ &\qquad PP_{\text{cogging}} \leq PP_{\text{coggінglimit}} \\ &\qquad t_{\text{rib}} \geq t_{\text{riblimit}} \end{aligned} \tag{7}$$

where PP_{cogging} is the peak-to-peak of the cogging torque, $PP_{\text{cogging limit}}$ is the limit value of PP_{cogging}, t_{tib} is the rib thickness, and $t_{\text{rib limit}}$ is the limit value of the rib thickness. The design variables for the stator chamfer and rotor notch structures are shown in Fig. 12. As in the first optimization process, the DOE was performed on the design variables of the second optimization, and the number of sample points was determined to be 144. In the second optimization, the proposed optimum model was determined using the Kriging surrogate model and SQP method. The structure of the proposed optimum model is shown in Fig. 13. Fig. 14(a) shows the waveform and fast Fourier transform (FFT) results for the no-load air-gap magnetic flux density of the optimally designed model calculated through FEA. The 3rd, 5th, and 7th harmonics of the proposed optimum model, to which the stator chamfer and rotor notch structures were applied, were reduced to 18.2%, 99.52%, and 53.14%,

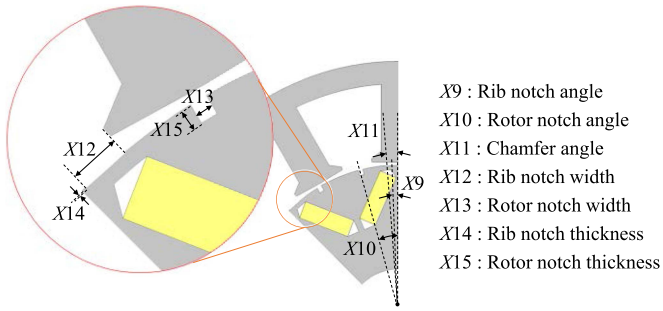

Fig. 12. Design variables in the second optimization [1].

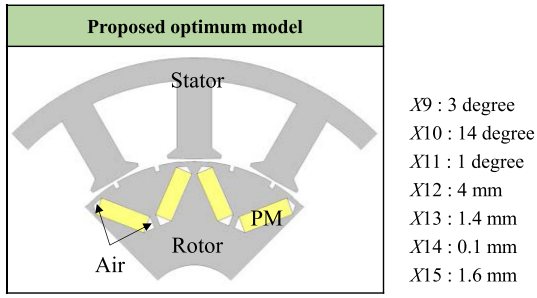

Fig. 13. Structure of the proposed optimum model [1].

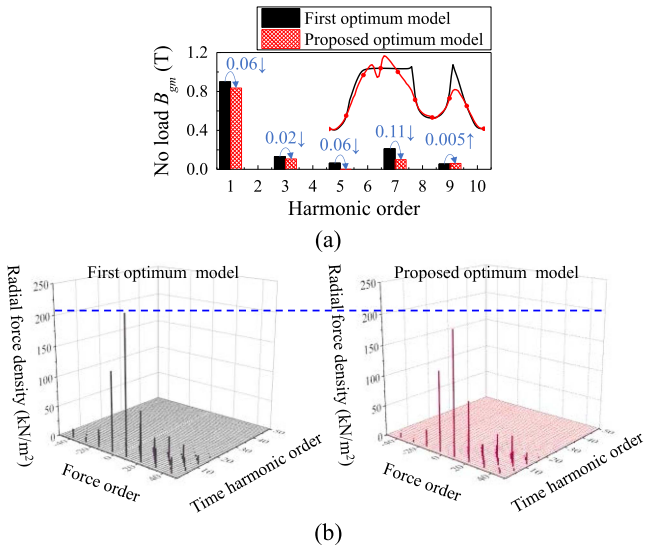

Fig. 14. (a) FFT results of no-load air-gap flux density. (b) Radial air-gap electromagnetic force density spectrum.

respectively, compared to the first optimum model. As the rib thickness of the rotor is limited in consideration of stiffness and manufacturability, the fundamental component of the no-load air-gap magnetic flux density of the proposed optimum model was reduced. However, the proposed optimum model satisfies the target torque while improving the harmonic characteristics within limited electrical specifications. In addition, the radial air-gap electromagnetic force density (AEFD), which affects the vibration and noise of the motor, is also reduced by the stator chamfer. Fig. 14(b) shows the radial AEFD spectrum of

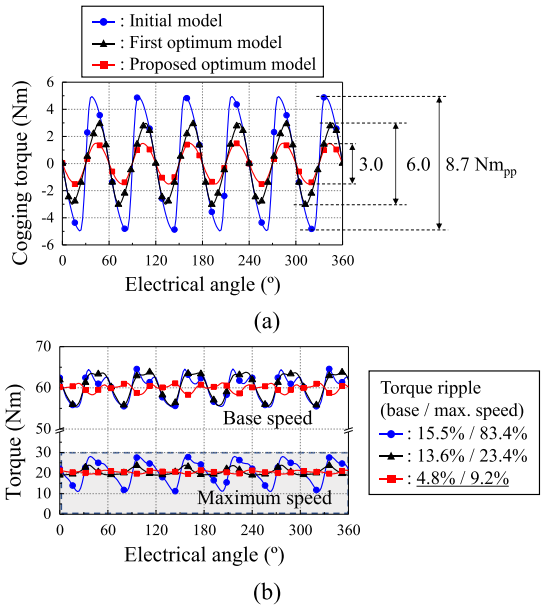

Fig. 15. Comparison of torque by models: (a) cogging torque and (b) torque at the base and maximum speed.

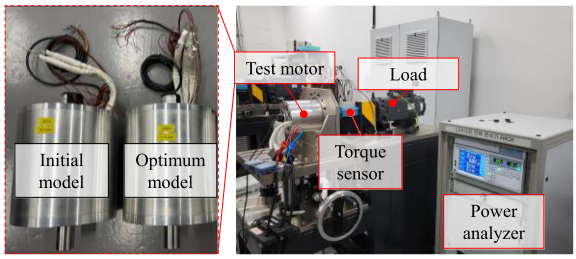

Fig. 16. Prototypes and experimental setup for the test of prototypes.

the first optimum model and the proposed optimum model at maximum torque and base speed. In an 8-pole 12-slot motor, when the time harmonic order is 2, the AEFD has the largest amplitude and the force order by the PM field is 8. At the time harmonic order of 2 and the force order of 8, the radial AEFDs are 222.6 kN/m^2 and 197.7 kN/m^2 in the first optimum model and proposed optimum model, respectively. As can be seen in Fig. 15(a), the peak-to-peak of the cogging torque for the first optimization model and proposed optimum model is 6.0 Nm$_{pp}$, 3.0 Nm$_{pp}$. Fig. 15(b) shows the torque at the base and maximum speed. The torque ripple at base and maximum speed is the smallest in the proposed optimum model.

IV. Experimental Verification

Through the proposed design process, the efficiency of the MOPs and harmonic characteristics of the proposed optimum model were improved compared with the initial model. Prototypes of the initial and proposed optimum models were realized to verify the validity of the design method. The experimental setup for load tests is shown in Fig. 16.

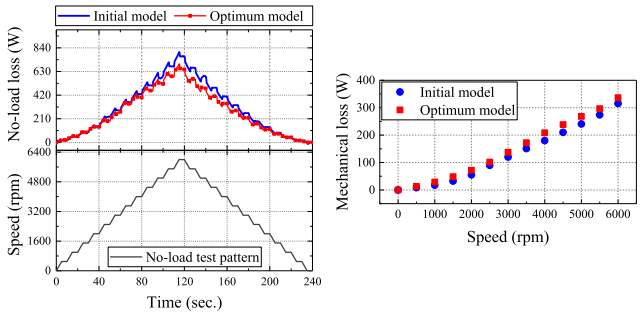

Fig. 17. (a) No-load test pattern and no-load loss. (b) Mechanical loss of prototypes.

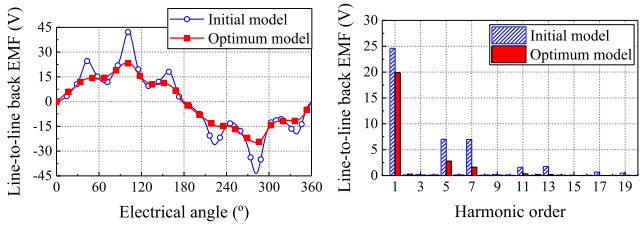

Fig. 18. Experimental no-load line-to-line BEMF: (a) waveform and (b) FFT results.

A. No-Load Test

The no-load test of each model was performed to estimate the mechanical loss at the speed pattern shown in Fig. 17(a). The room temperature was 25 °C. The mechanical loss causes an efficiency discrepancy between the experimental and theoretical. Since iron loss and copper loss occur due to magnetic field change by PM field at no-load, the mechanical loss in Fig. 17(b) is estimated by considering no-load iron loss and copper loss from the measured no-load loss [35]. As result, the mechanical loss of the optimum model with stator chamfer and rotor notch structures is estimated to be larger. Therefore, the efficiency reflecting the mechanical loss is calculated. Also, the harmonic of the no-load air-gap magnetic flux density are related to the harmonic components of the back electromotive force (BEMF) through a proportional relationship as

$$E_v \propto \frac{B_{v-\mathrm{th}}}{v} L_{stk} \tag{8}$$

where v is the harmonic order, $B_{v\text{-th}}$ is the amplitude of the v-th no-load air-gap magnetic flux density harmonics, and L_{stk} is the stack length. The BEMF measurement test is performed at a rotational speed 1000 rpm. Fig. 18 shows the BEMF measured by the no-load test, and the harmonic component of the BEMF of the optimum model is reduced compared to the initial model.

B. Load Test

The load test was performed to measure the efficiency at MOPs. To measure the efficiency at MOPs, the torque of the test motor is controlled, and the speed of the load is controlled. Table III lists the cable resistance connecting the power analyzer, the controller, and the motor, and the phase resistances of the prototypes. Since the phase resistance of motor is small, the cable

TABLE III
MEASURED PHASE AND CABLE RESISTANCE

Parameter	*Initial model*	*Optimum model*
Phase resistance (mΩ)	3.43	2.78
Cable resistance (mΩ)	6.53	

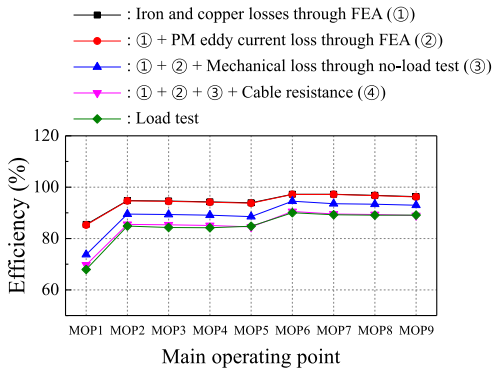

Fig. 19. Efficiency at MOPs of proposed optimum model.

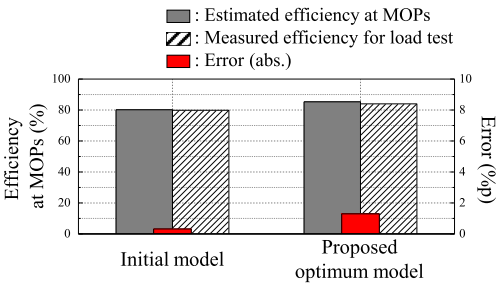

Fig. 20. Comparison of efficiency at MOPs.

resistance affects the motor efficiency. The estimated efficiency at MOPs, which reflects the electromagnetic losses (such as iron, armature copper, and PM eddy current losses), mechanical loss, and cable resistance, was compared by test results, as shown in Fig. 19. In Fig. 20, comparing the efficiency at the MOPs, the proposed optimum model was 84.0%, the initial model was 79.8%. Through the proposed design process, the efficiency at the MOPs of the motor increased by 4.2%p. The efficiency at MOPs evaluated using the load test is in good agreement (maximum error 1.8%p) with the efficiency at MOPs estimated with FEA and no-load test.

V. CONCLUSION

In this study, a two-step optimum design was developed to improve the efficiency of the MOPs and harmonic characteristics. Compared with the initial model, the proposed optimum model has higher efficiency at the MOPs and improved harmonic characteristics. The two-step optimization can shorten the computation time required for design. As a result, the proposed design process can be used to improve the efficiency at the MOPs and harmonic characteristics of the traction IPMSMs with a shortened design time.

REFERENCES

[1] S.-Y. Im, K.-S. Cha, Y.-J. Won, Y. Choi, and M.-S. Lim, "Optimum design applying stator chamfer and rotor notch structure to improve harmonics of high-driving efficiency electric vehicle," in *Proc. IEEE Transp. Electrific. Conf. Expo*, 2022, pp. 403–408, doi: 10.1109/ITEC53557.2022.9813766.
[2] P. Barman and B. Azzopardi, "Energy efficient torque allocation design emphasis on payload in a light-duty distributed drive electric vehicle," *IEEE Access*, vol. 9, pp. 118684–118695, 2021.
[3] M.-R. Park, D.-M. Kim, Y.-H. Jung, and M.-S. Lim, "High energy efficiency oriented-control and design of WFSM based on driving condition of electric vehicle," *Mechatronics*, vol. 81, 2022, Art. no. 102696.
[4] M. L. De Klerk and A. K. Saha, "A comprehensive review of advanced traction motor control techniques suitable for electric vehicle applications," *IEEE Access*, vol. 9, pp. 125080–125108, 2021.
[5] X. Liu, H. Chen, J. Zhao, and A. Belahcen, "Research on the performances and parameters of interior PMSM used for electric vehicles," *IEEE Trans. Ind. Electron.*, vol. 63, no. 6, pp. 3533–3545, Jun. 2016.
[6] X. Sun, Z. Shi, G. Lei, Y. Guo, and J. Zhu, "Analysis and design optimization of a permanent magnet synchronous motor for a campus patrol electric vehicle," *IEEE Trans. Veh. Technol.*, vol. 68, no. 11, pp. 10535–10544, Nov. 2019.
[7] F. Ma, H. Yin, L. Wei, G. Tian, and H. Gao, "Design and optimization of IPM motor considering flux weakening capability and vibration for electric vehicle applications," *Sustainability*, vol. 10, no. 5, May 2018, Art. no. 1533.
[8] Y.-H. Jung, M.-S. Lim, M.-H. Yoon, J.-S. Jeong, and J.-P. Hong, "Torque ripple reduction of IPMSM applying asymmetric rotor shape under certain load condition," *IEEE Trans. Energy Convers.*, vol. 33, no. 1, pp. 333–340, Mar. 2018.
[9] M. Kobayashi, S. Morimoto, M. Sanada, and Y. Inoue, "Design of notches on rotor surface to minimize cogging torque in dual-layered IPMSM by optimizing squared gap flux density waveform," in *Proc. IEEE Energy Convers. Congr. Expo.*, 2021, pp. 4171–4175.
[10] G.-J. Park, Y.-J. Kim, and S.-J. Jung, "Design of IPMSM applying V-shape skew considering axial force distribution and performance characteristics according to the rotating direction," *IEEE Trans. Appl. Supercond.*, vol. 26, no. 4, Jun. 2016, Art. no. 0605205.
[11] J.-W. Jung, D.-J. Kim, J.-P. Hong, G.-H. Lee, and S.-M. Jeon, "Experimental verification and effects of step skewed rotor type IPMSM on vibration and noise," *IEEE Trans. Magn.*, vol. 47, no. 10, pp. 3661–3664, Oct. 2011.
[12] G. H. Kang, Y. D. Son, G. T. Kim, and J. Hur, "A novel cogging torque reduction method for interior-type permanent-magnet motor," *IEEE Trans. Ind. Appl.*, vol. 45, no. 1, pp. 161–167, Jan./Feb. 2009.
[13] J. Wang, W. Geng, J. Guo, L. Li, and Z. Zhang, "Design and performance comparison of novel flux-concentrating IPM machines for power generation system application of extended-range electric vehicle," *IEEE Trans. Ind. Electron.*, vol. 70, no. 5, pp. 4450–4460, May 2023, doi: 10.1109/TIE.2022.3183341.
[14] H.-C. Jung, D.-J. Kim, S.-Y. Jung, and D. Lee, "Optimization method to maximize efficiency map of a drive motor with electrical winding changeover technique for hybrid EV," *IEEE Trans. Appl. Supercond.*, vol. 30, no. 4, Jun. 2020, Art. no. 5205405.
[15] D. Winterborne, N. Stannard, L. Sjöberg, and G. Atkinson, "An air-cooled YASA motor for in-wheel electric vehicle applications," *IEEE Trans. Ind. Appl.*, vol. 56, no. 6, pp. 6448–6455, Nov./Dec. 2020.
[16] J. Ruan and Q. Song, "A novel dual-motor two-speed direct drive battery electric vehicle drivetrain," *IEEE Access*, vol. 7, pp. 54330–54342, 2019.
[17] F. Momen, K. Rahman, and Y. Son, "Electrical propulsion system design of Chevrolet Bolt battery electric vehicle," *IEEE Trans. Ind. Appl.*, vol. 55, no. 1, pp. 376–384, Jan./Feb. 2019.
[18] J. Wang, W. Geng, Q. Li, L. Li, and Z. Zhang, "A new flux-concentrating rotor of permanent magnet motor for electric vehicle application," *IEEE Trans. Ind. Electron.*, vol. 69, no. 11, pp. 10882–10892, Nov. 2022.
[19] A. Dalal and P. Kumar, "Design, prototyping, and testing of a dual-rotor motor for electric vehicle application," *IEEE Trans. Ind. Electron.*, vol. 65, no. 9, pp. 7185–7192, Sep. 2018.
[20] T.-A. Huynh, P.-H. Chen, and M.-F. Hsieh, "Analysis and comparison of operational characteristics of electric vehicle traction units combining two different types of motors," *IEEE Trans. Veh. Technol.*, vol. 71, no. 6, pp. 5727–5742, Jun. 2022.
[21] X. Sun, Z. Shi, Y. Cai, G. Lei, Y. Guo, and J. Zhu, "Driving-cycle oriented design optimization of a permanent magnet hub motor drive system for a four-wheel-drive electric vehicle," *IEEE Trans. Transp. Electrific.*, vol. 6, no. 3, pp. 1115–1125, Sep. 2020.

[22] H. E. Perez, J. B. Siegel, X. Lin, A. G. Stefanopoulou, Y. Ding, and M. P. Castanier, "Parameterization and validation of an integrated electrothermal LFP battery model," in *Proc. ASME Dynamic Syst. Control Conf.*, 2012, pp. 1–10.
[23] M. Khayamy and H. Chaoui, "Current sensorless MTPA operation of interior PMSM drives for vehicular applications," *IEEE Trans. Veh. Technol.*, vol. 67, no. 8, pp. 6872–6881, Aug. 2018.
[24] D.-M. Kim, S.-Y. Lee, D.-K. Kim, M.-R. Park, and M.-S. Lim, "Sizing and optimization process of hybrid electric propulsion system for heavy-duty vehicle based on Gaussian process modeling considering traction motor characteristics," *Renewable Sustain. Energy Rev.*, vol. 161, 2022, Art. no. 112286.
[25] S. Kim, S.-G. Lee, J.-M. Kim, T. H. Lee, and M.-S. Lim, "Robust design optimization of surface-mounted permanent magnet synchronous motor using uncertainty characterization by bootstrap method," *IEEE Trans. Energy Convers.*, vol. 35, no. 4, pp. 2056–2065, Dec. 2020.
[26] G. Lei, T. Wang, Y. Guo, J. Zhu, and S. Wang, "System-level design optimization methods for electrical drive systems: Deterministic approach," *IEEE Trans. Ind. Electron.*, vol. 61, no. 12, pp. 6591–6602, Dec. 2014.
[27] N. Taran, D. M. Ionel, and D. G. Dorrell, "Two-level surrogateassisted differential evolution multi-objective optimization of electricmachines using 3-D FEA," *IEEE Trans. Magn.*, vol. 54, no. 11, Nov. 2018, Art. no. 8107605.
[28] H. Kim et al., "Efficient design optimization of complex system through an integrated interface using symbolic computation," *Adv. Eng. Softw.*, vol. 126, pp. 34–45, Dec. 2018.
[29] C. T. Lawrence and A. L. Tits, "A computationally efficient feasible sequential quadratic programming algorithm," *Soc. Ind. Appl. Math.*, vol. 11, no. 4, pp. 1092–1118, 2001.
[30] Z. Shi et al., "Torque analysis and dynamic performance improvement of a PMSM for EVs by skew angle optimization," *IEEE Trans. Appl. Supercond.*, vol. 29, no. 2, Mar. 2019, Art. no. 0600305.
[31] L. R. Huang, J. H. Feng, S. Y. Guo, Y. F. Li, J. X. Shi, and Z. Q. Zhu, "Rotor shaping method for torque ripple mitigation in variable flux reluctance machines," *IEEE Trans. Energy Convers.*, vol. 33, no. 3, pp. 1579–1589, Sep. 2018.
[32] D. Wang, X. Wang, and S.-Y. Jung, "Reduction on cogging torque in flux-switching permanent magnet motor by teeth notching schemes," *IEEE Trans. Magn.*, vol. 48, no. 11, pp. 4228–4231, Nov. 2012.
[33] H. Dhulipati, S. Mukundan, K. L. V. Iyer, and N. C. Kar, "Skewing of stator windings for reduction of spatial harmonics in concentrated wound PMSM," in *Proc. IEEE 30th Can. Conf. Elect. Comput. Eng.*, 2017, pp. 1–4, doi: 10.1109/CCECE.2017.7946834.
[34] X. Ge, Z. Q. Zhu, G. Kemp, D. Moule, and C. Williams, "Optimal step-skew methods for cogging torque reduction accounting for three-dimensional effect of interior permanent magnet machines," *IEEE Trans. Energy Convers.*, vol. 32, no. 1, pp. 222–232, Mar. 2017.
[35] N. Taran, D. M. Ionel, V. Rallabandi, G. Heins, and D. Patterson, "An overview of methods and a new three-dimensional FEA and analytical hybrid technique for calculating AC winding losses in PM machines," *IEEE Trans. Ind. Appl.*, vol. 57, no. 1, pp. 352–362, Jan./Feb. 2021.

So-Yeon Im received the bachelor's degree in automotive engineering from Hanyang University, Seoul, South Korea, in 2020, where she is currently working toward the Ph.D. degree in automotive engineering. Her research interests include optimization, design, and system modeling of electric vehicles.

Kyoung-Soo Cha received the bachelor's degree in electric engineering from Chungbuk University, Cheongju, South Korea, in 2015, and the Ph.D. degree in automotive engineering from Hanyang University, Seoul, South Korea, in 2022. In 2022, he was a Postdoctoral Researcher at Hanyang University. Since 2022, he has been with the Korea Institute of Industrial Technology, Daegu, South Korea, where he is currently a Postdoctoral Reseacher. His research interests include electric machine design for automotive and home appliance, system modeling and optimization of electric vehicles, hybrid electric vehicle, and fuel cell electric vehicles.

Yun-Jae Won (Graduate Student Member, IEEE) received the bachelor's degree in automotive engineering from Hanyang University, Seoul, South Korea, in 2021, where he is currently working toward the Ph.D. degree in automotive engineering. His research interests include design, vibration, and noise analysis of electric machines.

Yun-Yong Choi received the Ph.D. degree in automotive engineering from Hanyang University, Seoul, South Korea, in 2017. He is currently the CEO of DRIVETECH, a technology venture. His research interests include design and product technical development of electric drive system.

Myung-Seop Lim (Member, IEEE) received the bachelor's degree in mechanical engineering, the master's and the Ph.D. degrees in automotive engineering from Hanyang University, Seoul, South Korea, in 2012, 2014, and 2017, respectively. From 2017 to 2018, he was a Research Engineer at Hyundai Mobis, Yongin, South Korea. From 2018 to 2019, he was an Assistant Professor at Yeungnam University, Daegu, South Korea. Since 2019, he has been with Hanyang University, where he is currently an Assistant Professor. His research interests include electromagnetic field analysis and multi-physics analysis of electric machinery for mechatronics system such as automotive and robot applications.